COMBINED HIGH FLUENCE AND HIGH CYCLE NUMBER TRANSIENT LOADING OF ITER-LIKE MONOBLOCKS IN MAGNUM-PSI

T.W. MORGAN[1,2,*], Y. LI[1,3], M. BALDEN[4], S. BREZINSEK[5], G. DE TEMMERMAN[6,7]

[1]*DIFFER - Dutch Institute for Fundamental Energy Research, De Zaale 20, 5612 AJ Eindhoven, the Netherlands*
[2]*Eindhoven University of Technology, Faculty of Applied Physics, Groene Loper 19, 5612 AP, Eindhoven, Netherlands*
[3]*Eindhoven University of Technology, Department of Mechanical Engineering, Groene Loper 3, 5612 AE, Eindhoven, Netherlands*
[4]*Max-Planck-Institut für Plasmaphysik, Boltzmannstr. 2, 85748 Garching, Germany*
[5]*Forschungszentrum Jülich, Institut für Energie- und Klimaforschung - Plasmaphyisk, 52425 Jülich, Germany*
[6]*Zenon Research, F-75006 Paris, France*
[7]*MINES ParisTech, University PSL, Institute of Higher Studies for Innovation and Entrepreneurship (IHEIE), 75006 Paris, France*

* Email: t.w.morgan@differ.nl

Keywords: ITER-monoblocks, tungsten, ELM-loading, high-fluence, Magnum-PSI

Abstract

It is highly desirable to understand the long term evolution of the divertor material under the extreme steady-state and transient heat and particle loads expected during ITER operation. Here the impact of ELM-like transient loading under combined high-flux plasma and transient ELM-like heat loading in Magnum-PSI was explored to determine how plasma affects the fatigue cracking threshold of tungsten due to ELMs. Mock-ups consisting of five ITER-like monoblocks in a chain were simultaneously exposed to high flux plasma and a high power pulsed laser which closely simulated the ELM impact in terms of heat flux and duration. Loading conditions were chosen to enable comparison to existing data from electron-beam loading, while the influence of surface base temperature (750 °C, 1150 °C or 1500 °C) and impurity seeding (addition of 6.5 ion% He^+ and/or 8 ion% Ne^+) were also investigated. The plasma loading leads to differences in surface morphology and indicates synergistic effects on the extent of the surface damage. Base temperatures at or above 1150 °C are found to lead to a significant reduction in the fatigue cracking threshold by a factor of two or more compared to at 750 °C. Cracked surfaces are found to be more than ten times rougher than the original microstructure, and additionally when seeding impurities are added surface roughness can be significantly increased by up closely factor of two compared to roughening using pure H plasma. Overall the results indicate that avoiding fatigue cracking in ITER will be very challenging, and that understanding the level to which this can therefore be tolerated is vital for anticipating divertor lifetime and reliability.

1. INTRODUCTION

The achievement of the ITER project is strongly reliant on the successful performance of the ITER tungsten divertor, and holding the loading onto the divertor surfaces to tolerable limits gives one of the strongest constraints on how the tokamak is operated [1, 2]. Recent multi-machine scaling gives a good regression to estimate the parallel energy loads ($\varepsilon_{||}$) expected for unmitigated type-I Edge Localized Mode (ELM) loads in ITER [3]. By taking this scaling and translating it into operational limits for the divertor it is implied that ELM mitigation is required to avoid net surface reshaping via toroidal gap edge melting [1, 2]. The tungsten surfaces are also vulnerable to surface crack-network development due to fatigue failure, as around 10^6 ELMs would be achieved in only around 100 baseline 400 s duration Fusion Power Operation (FPO) discharges in ITER, achievable in approximately one week's operation [2]. The energy density threshold for surface crack network formation is

significantly lower than toroidal gap edge melting [4]. A question therefore arises whether avoiding this would be the limiting factor for divertor survival to sufficient lifetime. It may be anticipated that surface microcracks could act as stress concentrators to increase the likelihood of self-castellation [5, 6], that the strong roughening created could increase erosion, or that grains or subgrains could become isolated which could be lost into the plasma or melt [4, 7]. Little data [8] exists on the influence of plasma loading on fatigue behaviour due to ELMs, however plasma loading and ELM loading both predominantly affect only a thin surface region, which suggests a synergy may occur which may enhance the damage effect. In particular, high fluence plasma conditions have only recently become available to explore [9], therefore in this paper we explored the influence of high-flux and high-fluence plasma loading on tungsten fatigue crack behaviour due to ELM-like heat loads simulated by laser-beam exposure.

2. METHODOLOGY

2.1. Monoblock mock-ups

Two monoblock mock-up chains (MUC1 and MUC2) manufactured by Research Instruments GmbH were used in this series of experiments, each consisting of five monoblocks following the ITER design specifications [10], each bonded to a single CuCrZr cooling pipe with an interlayer of copper. Each monoblock had surface dimensions of x=12 mm wide and y=28 mm long and had elongated tungsten grains in the surface normal (z) direction conforming to the ITER material specification [11]. The blocks were exposed “as received” apart from cleaning with water and alcohol, and had a rough surface due to the block milling process with a clear grooving as a result of this. The experiment consisted of five rounds of combined loading, the first using MUC1 and the subsequent four using MUC2. It was found after the first round that strong oxidation had occurred on the monoblock surfaces during welding of the pipe to the cooling connectors, and therefore the second chain was used for subsequent rounds and no welding was performed. However, the results presented here are not significantly affected by this as the H plasma removed the oxide at the exposure locations.

2.2. Experimental conditions

T_{base}	750 °C	1150 °C	1500 °C
Gas species	H, H+He, H+Ne, H+He+Ne	H, H+He, H+Ne	H, H+He, H+Ne
Γ_{peak} $(m^{-2}\ s^{-1})$	$3\text{-}3.5\times10^{24}$	$1.5\text{-}2.1\times10^{24}$	$1.2\text{-}4.3\times10^{24}$
Φ_{peak} (m^{-2})	$0.1\text{-}1.3\times10^{29}$	$1\text{-}1.4\times10^{28}$	$0.8\text{-}2.8\times10^{28}$
F_{HF} $(MW\ m^{-2}\ s^{0.5})$	2.6-12.9	3.7-5.8	3.7-5.8
N_{pulse}	$10^4\text{-}10^6$	4×10^5	4×10^5

Table 1: Summary of exposure parameters. Laser pulse duration was 1 ms with frequency of 10-80 Hz.

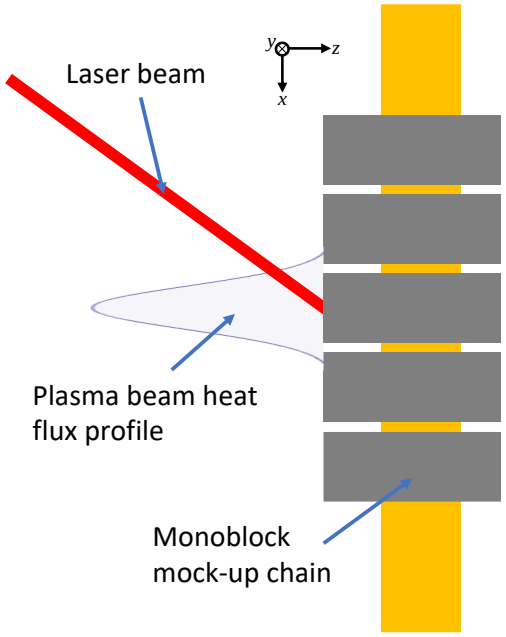

Figure 1:Schematic overview of the monoblock loading conditions. The plasma beam profile indicates the intensity profile of the heat and particle fluxes while the laser beam loaded a small oval region of the block. By changing the mounting height in the y direction and tilt of the blocks around the y-axis the height of the laser and plasma loading could be moved in the y and x direction respectively to load different regions of the mock-up chain.

Each chain was mounted on a tiltable and rotatable sample holder with high pressure water cooling (inlet temperature 22 °C, flow rate 4.8 m/s, pressure 2 MPa) and exposed to combined plasma and transient heat loading in the Magnum-PSI linear plasma device [12]. Although the cooling conditions differ from those in ITER, this produces a similar thermal gradient in the *z*-direction as would be expected in ITER and does not significantly influence the interpretation of the results presented here. The Magnum-PSI plasma beam has a Gaussian cross-section and in these experiments the typical full-width at half maximum (FWHM) of the beam was 11-14 mm. This is comparable to the width of each block and therefore a different exposure condition was chosen for each monoblock and could be treated as an independent surface loading (Figure 1). This was achieved by changing the tilt angle of the monoblock chain normal direction relative to the plasma beam axis from -15° to +11° in 6.5° intervals which effectively moved the position in the *x*-direction. By adjusting the height of the target holder and rotating the sample it was possible to position the plasma beam such that it was centred at different positions in the *y*-direction of each monoblock, enabling different rounds of exposure to be carried out on the same mock-up. Where possible the loading was carried out in a single long exposure to ensure that the laser spot location was kept in the same place throughout. Two occasions where this was not possible are noted in Table 2.

Simultaneously transient loading was applied using a 1064 nm Nd:YAG laser (LASAG FLS 352-302) with a pulse duration t = 1 ms and a frequency in the range of 10-80 Hz. The power density was varied between 80-410 MW m^{-2}. The laser spot was focused at the centre of the plasma beam in each case, typically with an accuracy of better than 2 mm relative to each other. The laser spot had an elliptic projection with semi-major and semi-

minor axes of 6.4 and 4.0 mm respectively, and a near square-wave time evolution. Therefore although this only locally loaded a small region of the monoblock each time, in terms of the microstructural modifications observations close to the centre of the laser spot can be expected to be representative of the effect of ELM-like heat loading (which would uniformly load the monoblock surface). This can be seen from the fact that the thermal gradient is largest in the *z* direction rather than the *x-y* directions due to the small heat penetration depth from the laser pulse (approximately 450 μm assuming a semi-infinite plane due to the short transient loading duration of 1 ms) relative to the temperature gradients in the *x-y* plane. Consequently therefore the thermal stresses are dominated by those into the material, which is the same as the case of uniform loading[13][14].

The plasma conditions were chosen to create a base surface temperature (T_{base}) at the plasma beam centre of either 750, 1150 or 1500 °C, with plasma temperatures ranging from 1-6 eV and densities from 0.5-5×10^{20} m^{-3}. These surface temperatures were chosen respectively as being above the ductile-to-brittle transition temperature (DBTT) for tungsten (300-400 °C [15, 16]) and similar to literature values on electron beam loading for comparison [7]; at a temperature where recovery should occur during plasma exposure; and at a temperature where recrystallization should occur during the plasma exposure [17, 18]. Additionally the plasma was chosen to be pure H, as a proxy for the fusion D-T mixture, or with the addition of He (representing the fusion reaction by-product) and/or Ne (a candidate seeding impurity for ITER). Rounds 1 and 2 used pure H plasma, while seeding impurities were added for Round 3 and a mixture of pure H plasma and seeded plasma were used in Rounds 4 and 5. The range of temperature increase (ΔT) and number of loading cycles (N_{pulse}) chosen for the laser for rounds 1 and 2 was selected over a range to be comparable to the chosen literature data [7]. The heat flux factor was determined from solving the one-dimensional heat equation as $F_{HF} = qt^{0.5} \propto \Delta T$ [19], where q is the power density absorbed by the surface from the laser pulse. The factor F_{HF} was then used to compare between electron-beam and laser loading results. For subsequent rounds (R3-R5) two conditions were chosen (($\Delta T = 200$, 310 °C, i.e. $F_{HF} = 3.7$, 5.8 MW m^{-2} $s^{0.5}$, $N_{pulse} = 4 \times 10^5$) which were found to be close to the threshold for fatigue cracking, and the influence of seeding impurity and base surface temperature on the fatigue cracking behaviour were explored. Additionally it may be considered that the number of pulses ($N_{pulse} = 4 \times 10^5$) is approximately equivalent to the number expected in one hundred 400 s ITER FPO discharges with an ELM frequency of 10 Hz. A summary of the exposure conditions can be found in Table 1 and are given in more detail in Table 2.

Round	*Monoblock number*									
	B1		*B2*		*B3*		*B4*		*B5*	
R1					750	H	750	H	750	H
					340	4.2×10^5	140	1.0×10^6	690	6.5×10^4
R2	750	H	750	H	750	H	750	H	750	H
	310	1.0×10^5	200	1.0×10^4	200	2.0×10^5	310	4.2×10^5	240	1.2×10^4
					200*	8.0×10^5*			320*	1.0×10^4*
R3	750	H/Ne	750	H/Ne	750	H/He/Ne	750	H/He	750	H/He
	200	4.0×10^5	310	4.0×10^5	200	4.0×10^5	310	4.0×10^5	200	4.0×10^5
R4	1150	H	1150	H	1150	H/He	1150	H/Ne	1150	H/Ne
	200	4.0×10^5	310	4.0×10^5	200	4.0×10^5	310	4.0×10^5	200	4.0×10^5
R5	1500	H	1500	H	1500	H/He	1500	H/Ne	1500	H/Ne
	200	4.0×10^5	310	4.0×10^5	200	4.0×10^5	310	4.0×10^5	200	4.0×10^5

*Table 2: Details of plasma and laser exposures for each round. The four parameters given are T_{base} (°C, top left), gas species used (top right), ΔT due to the laser pulse (°C, bottom left) and N_{pulse} (bottom right). The * indicates where two exposure conditions were made at near co-located positions due to issues of realignment following stoppages in the exposure.*

2.3. Experimental diagnostics

The plasma electron temperature (T_e) and density (n_e) was monitored using Thomson scattering, and the measurements at the plasma beam centre were used to determine the average peak plasma flux ($\langle \Gamma_{pk} \rangle$) and peak plasma fluence (Φ_{pk}) using the Bohm criterion as in [9]. Experiments were carried out with samples electrically floating.

The base temperature was monitored using a single-chord multi-wavelength pyrometer (FAR-Associates FMPI Spectropyrometer) while the ΔT due to the heat pulses was monitored using a fast infra-red (IR) camera (FLIR SC7500MB, 3.97-4.01 μm, 4856 Hz). The pyrometer results were used to calibrate the base temperature of the IR camera as in [20].

The seeding impurities in the plasma were determined using survey optical emission spectroscopy (OES, Avantes AvaSpec-2048-USM2-RM) in the range 299-950 nm with a viewing chord focused on the target surface at the plasma beam centre at a viewing angle of 40° to the surface normal. The seeding impurity ion fraction of species x ($f_x = n_{x^+}/n_{H^+}$) was determined using the line ratio method described in [9]. The following emission lines were used: H: 410 nm, 388 nm; He: 587 nm, 668 nm; Ne: 640 nm, 650 nm. This gives four line pairs in each case for He/H and Ne/H and from which an uncertainty was determined based on the range of values determined. For the chosen gas flow ratios the resultant ion impurity fractions were $f_{He} = 6.5 \pm 2\%$ and $f_{Ne} = 8.0 \pm 2\%$ in the cases where seeding impurities were used.

2.4. Pre- and post-mortem investigation

A goal of the experiment was to examine the effects of the combined loading by looking for changes in the surface morphology. Therefore plasma loading sites were pre-chosen and pre-characterized for rounds 1-4. For round 5 no pre-examination of the surface was carried out. The exposed sites were then subsequently analysed. In some cases due to the challenge of aligning the plasma beam and laser these sites were not co-located with the pre-characterized locations.

Characterization using scanning electron microscopy (SEM) on the surface and focused ion-beam (FIB) milled cross-sections was carried out using a ZEISS "Auriga60" SEM equipped with Canon ion gun and a unique stage from KAMMRATH&WEISS for large and heavy samples. This is capable of mounting and examining the entire monoblock chain without cutting sub-samples, permitting this stepwise examination approach. Additionally energy dispersive X-ray spectroscopy (EDX) was used to monitor the surface elemental composition in this setup.

Overview surface imaging and the surface height (Z) was measured using confocal laser scanning microscopy (CLSM) (LEXT OSL4000, OYMPUS). More information about the Auriga and CLSM setups can be found in [21]. From the surface height the route-mean squared surface roughness was determined as

$$S_q = \sqrt{\frac{1}{A}\iint Z^2(x,y)\mathrm{d}x\mathrm{d}y} \quad (1)$$

where $A = 0.16$ mm^2 is the area averaged over. The initial surface root mean square roughness for MUC2 was 1.48±0.26 μm.

3. RESULTS AND DISCUSSION

3.1. The influence of H-plasma on ELM-like fatigue damage

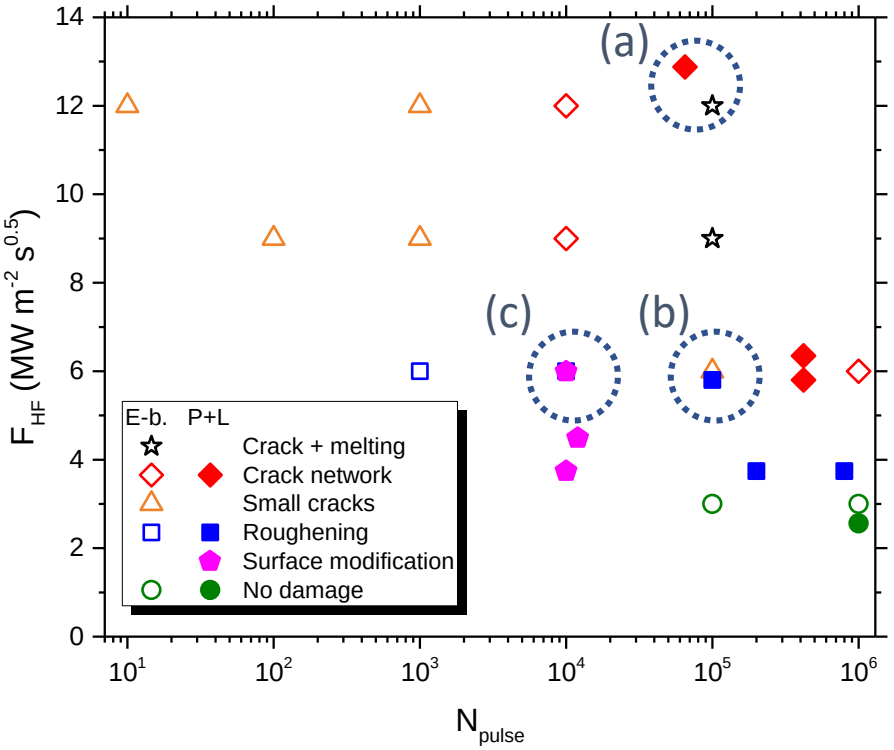

Figure 2: Summary of exposures categorized by damage type for plasma and laser loading from rounds 1&2 (P+L, filled symbols) compared with similar electron-beam loading results from [7] *(E-b, empty symbols). A description of the damage categories is given in section 3.1. The circles labelled (a)-(c) highlight the conditions where discrepancies between E-b and P+L loading were identified and correspond to the labels of Figure 3.*

The results of the experiments using combined plasma and laser loading (P+L) in rounds 1 and 2 are summarized in Figure 2 and plotted together with literature data on electron-beam (E-b) loading taken from [7]. Here the samples were exposed at comparable temperatures (700 °C), with "ITER-grade" tungsten of similar grain orientation and texture, which permits direct comparison between the two. The damage categories are mostly defined in [7]: 'Roughening' is defined by a clear increase in surface roughness compared to the original surface, 'Small cracks' are defined as intergranular cracks formed over one or several grain boundaries but not connected to each other. If they do interconnect this is defined as a 'Crack network'. 'Crack and melting' defines a crack network where additionally small isolated regions have melted on individual grain. Additionally we list here 'Surface modification' of corrugation and "erosion lines", which are discussed in more detail below and shown in Figure 3(c). Overall the results are very similar, with comparable thresholds where no damage is observed and where crack networks are observed to form. Some discrepancies are noted however, and are discussed here.

Firstly, it can be observed that at comparable high loading and cycle numbers (P+L: $F_{HF} = 12.9$ MW m^{-2} s$^{0.5}$, $N_{pulse} = 6.5 \times 10^4$; E-b: $F_{HF} = 12.0$ MW m^{-2} s$^{0.5}$, $N_{pulse} = 1 \times 10^5$) no melting is observed in the P+L case (Figure 3(a)). For the electron beam experiments it was observed that sub-grain size regions (~10 µm diameter) had melted, typically located at protruding regions of the strongly roughened and cracked surfaces. This was explained by thermal isolation of these regions due to the surface cracking process, which additionally indicates a loose contact which could increase the risk of erosion [4]. Here no such melted regions were observed, and overall the surface appears with a more "cauliflower-like appearance", despite the strongly roughened and cracked

surface, compared to the E-b data point. This suggests a difference in the way the energy from the electron beam and laser beam are coupled into the surface, or a synergy with the plasma which "rounds" the cracked edges before they can become isolated enough to form melt regions, though the mechanism for this is unclear as the ion energy of the H plasma, and even for any heavy trace impurities, was below the sputtering threshold. However, the plasma may also be acting to enhance surface adatom migration which could give rise to these differences [22], though the presence of surface defects and high roughness would counteract this. Alternatively, the difference could arise from an electron-beam effect: as the surface cracks the electrons can penetrate deeper and the electron reflection coefficient thus is altered. If, locally, the reflection coefficient was reduced, this could result in local overheating and melting in the e-beam case. In the P+L case the changes to emissivity were compensated by tracking the surface temperature using the pyrometer of Magnum-PSI, and therefore this effect should not occur and would also not be anticipated in a ELM plasma-loading situation.

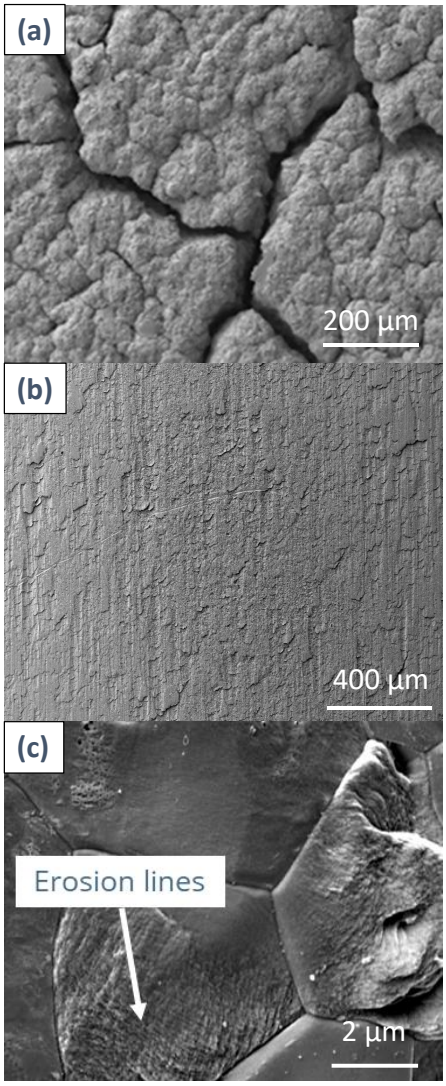

Figure 3: Microstructure of surface after different exposure combinations. The figure letter refers to the condition labelled in Figure 2.

Secondly for cases of medium loading and high cycle numbers (P+L: $F_{HF} = 5.8$ MW m^{-2} s$^{0.5}$, $N_{pulse} = 1 \times 10^5$; E-b: $F_{HF} = 6.0$ MW m^{-2} s$^{0.5}$, $N_{pulse} = 1 \times 10^5$) small cracks were observed in the E-b case. In the P+L case these were not observed (Figure 3(b)). This is attributed to the as-received surface in this case, compared to the polished surface used in [7]. Either these small cracks are present, but unobservable due to the rough surface, or the rough surface is more able to plastically deform and thus has a higher tolerance before such cracks are formed. In metals like steel or aluminium alloys higher roughness typically results in lower fatigue strength due to higher stress concentration and higher residual stresses [23–25]. This does not seem to be the case here, however

overall this advantage seems marginal as the threshold for full crack network formation appears to be similar in both cases.

Thirdly, for cases with low to medium power loading but low cycle numbers (P+L: $F_{HF} = 5.8$ MW m^{-2} s$^{0.5}$, $N_{pulse} = 1 \times 10^4$; E-b: $F_{HF} = 6.0$ MW m^{-2} s$^{0.5}$, $N_{pulse} = 1 \times 10^4$), the P+L cases observe clear plasma modifications: corrugation and stepped "erosion lines" on certain grains, which are not observed in the electron-beam case (Figure 3(c)). These are typically caused by a combination of sputtering and adatom migration processes. The features are only seen in the region which was subjected to combined loading. This may be attributed to the exponential temperature dependence of the adatom diffusion along different crystallographic directions, which only results in unstructured roughened morphologies at lower temperatures in metals [26].

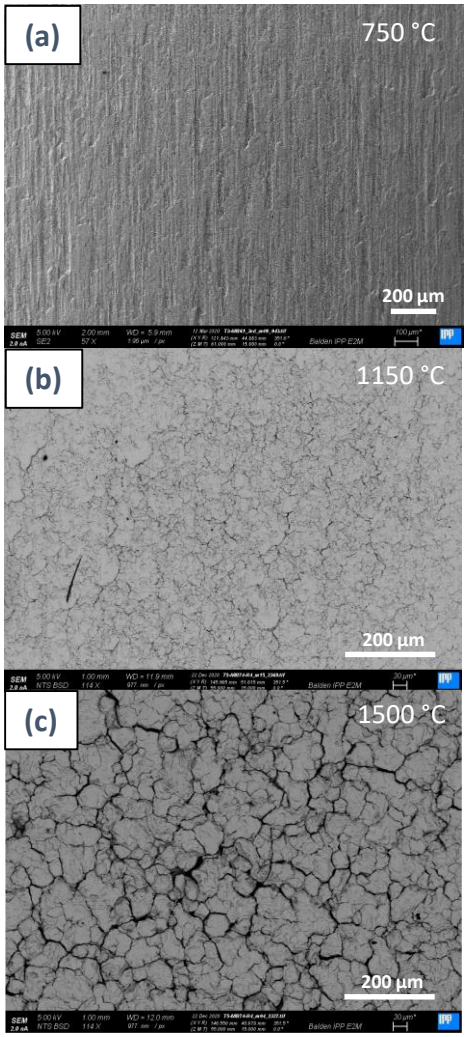

Figure 4: SEM images of the monoblock microstructure following exposure with H plasma at $F_{HF} = 3.7$ MW m^{-2} s$^{0.5}$, $N_{pulse} = 4 \times 10^5$ with T_{base} = 750 °C (a), 1150 °C (b) or 1500 °C (c).

3.2. The influence of surface temperature on ELM-like fatigue damage

In rounds 4 and 5 pure H plasmas were used to compare damage morphology at different base temperatures but identical pulse number and with two different heat loading conditions (R4&R5, B1&B2 were compared to R2, B3&B4). At 750 °C, for the lower of these two heat flux factors ($F_{HF} = 3.7$ MW m^{-2} s$^{0.5}$, $N_{pulse} = 4 \times 10^5$) only roughening was observed, while for the higher case ($F_{HF} = 5.8$ MW m^{-2} s$^{0.5}$, $N_{pulse} = 4 \times 10^5$) a crack network was found to form (Figure 2). However at the higher base temperatures (1150 °C and 1500 °C) a crack

network forms even for the lower power case (Figure 4). Additionally the crack network is more extensive with more pronounced grain boundary separation in the latter case.

In order to understand this behaviour the Coffin-Manson relationship [27, 28] was applied to understand the crack initiation behaviour of the surface under cyclical loading at different temperatures. For samples undergoing uniaxial compression/tension loading tests the number of cycles to failure (N_f) is related to the plastic strain amplitude ($\Delta\varepsilon^p/2$) by

$$\frac{\Delta\varepsilon^p}{2} = \varepsilon_f^{'} \left(2N_f\right)^c \quad (2)$$

where $\varepsilon_f^{'}$ is the fatigue ductility coefficient and c is the fatigue ductility exponent. These were empirically determined from measured fatigue data of tungsten at 815 °C [29] and 1232 °C [30]. Making the assumption that these constants are still appropriately close to values at respectively 750 °C and 1150 °C, and equating $N_f = N_{cycles}$ it is only left to relate $\Delta\varepsilon^p/2$ to F_{HF}. This was done by using Finite Element Method modelling with MSC.Marc/Mentat® using a methodology described in more detail in [20]. In this case the observed temperature response due to a pulse was modelled to fit the observed IR camera images and then from the model the plastic strain per cycle was determined. The model was also used to correlate this to F_{HF}. From this the observed data can be compared to expectations from the Coffin-Manson relationship, as presented in Figure 5. It can be observed firstly that the prediction from the model matches the data relatively well, generally reproducing the cracking threshold boundary, particularly considering the model was developed for uniaxial fatigue, rather than surface fatigue testing (biaxial stress state) and that the material was not identical (recrystallized compared to forged W). Secondly the model also reproduces the observed reduction in F_{HF} required to lead to cracking at higher temperatures. This can be qualitatively explained by the observation that the tungsten yield and tensile strength both strongly reduce as a function of temperature due to higher dislocation mobility at higher temperatures [31–33]. This increases ductility but also makes it easier to accumulate plastic deformation and creep in the plastic zone of the fatigue crack [34]. Therefore it can be expected that tungsten will accumulate fatigue damage at a higher rate at elevated temperatures. The more pronounced grain boundary separation for the case where recrystallization took place (1500 °C, Figure 4(c)) indicates an even lower threshold for crack network initiation, in line with recent observations where the increase in high angle grain boundary fraction and decrease in defect density which occur during recrystallization are also found to be contributory factors [20].

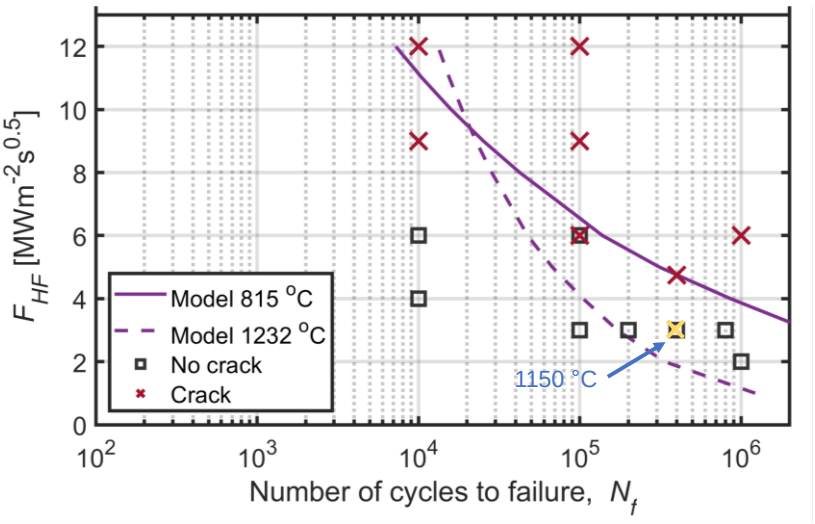

Figure 5: Simplified version of the data from Figure 2 indicating whether cracking occurred or not, overlaid with the calculated Coffin-Manson relationship. All data (black squares and red crosses) are recorded at a base temperature of 750 °C. except for the yellow cross indicated by the arrow, which is the additional data point at which cracking occurs measured at 1150 °C

3.3. The influence of seeding impurities on ELM-like fatigue damage

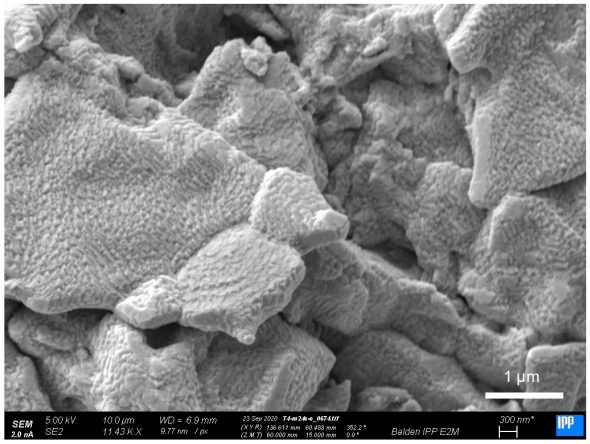

Figure 6: SEM image of the laser loaded region of R3;B2: Gas Species = H+Ne, T_{base}=750 °C, N_{pulse}=4×10^5, ΔT=310 °C, which shows the additional edge nanostructures which were formed.

In round 3 seeding impurities were added to compare to rounds 1 and 2 while keeping the base temperature at 750 °C. Overall no difference was found in the damage category achieved which were indicated for pure H in Figure 2. However small differences could be observed when looking in detail at the microstructure for the exposures with H+Ne, where nm scale edge nanostructures could be observed over the surface (Figure 6). These were a more extensive version of the phenomena described in section 3.1 which extended over all grains rather than just a few. For the cases with H+He and the single case of H+He+Ne no significant nanostructuring was observed.

The emissivity of the surface at the laser-loaded spot was tracked by comparing the IR camera and pyrometer signals between laser pulses. The results of this can be observed in Figure 7 for all cases with $T_{base} =$ 750 °C, i.e. R1-R3. The initial emissivity was typically 0.2. Generally, but not always, the emissivity is found to gradually increase with time. Two things can be derived from this. Firstly the increase in emissivity is generally lower for $\Delta T = 200$ rather than 310 °C, which likely correlates to the lower rate of roughening at lower heat flux factor. Secondly, that the case of H+Ne at $\Delta T = 310$ °C has a much higher rate of emissivity increase. This may possibly be related to the nanostructuring effect seen in Figure 6.

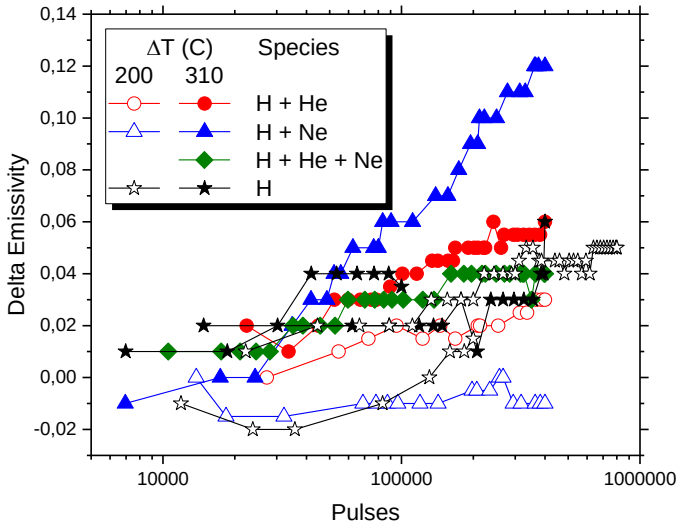

Figure 7: Evolution of the change in the surface emissivity of the laser-loaded region with laser pulse number.

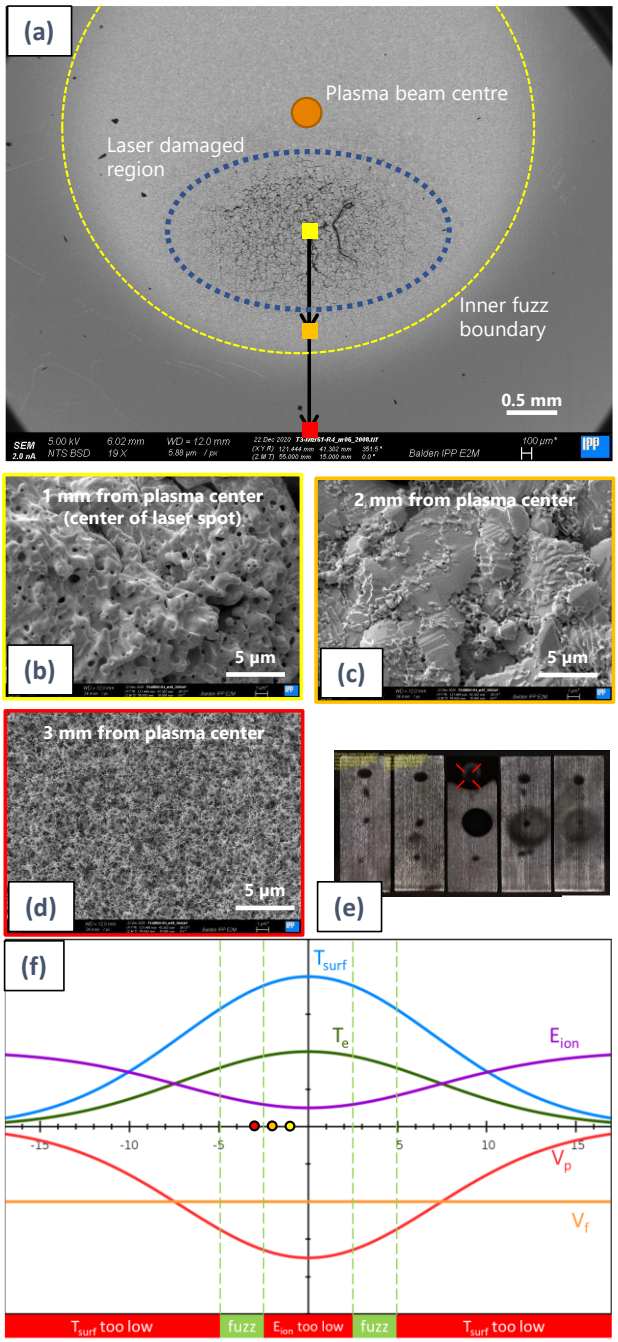

Figure 8: (a) SEM overview of the plasma and laser spot center for the case R5;B3: Gas Species = H+He, T_{base}=1500 °C, N_{pulse}=4×10^5, ΔT=310 °C. The dark ring indicates the region where fuzz has formed. The laser damaged region is indicated with a blue dotted ring.; (b)-(d) SEM images focused on positions 0 (b), 1 (c) and 2 (d) mm from the laser spot position, as indicated in (a); (e) overview of the entire MUC2 with the red cross indicating where the SEM image (a) was located; (f) sketch (made with graphsketch.com) of representative radial profiles along the target (mm) of surface temperature (T_{surf}), electron temperature (T_e), target floating potential (V_f), plasma potential (V_p) and ion energy (E_{ion}) indicating the region where fuzz would be expected to form in Magnum-PSI (neglecting the laser loading in this case). The three coloured dots represent the radial positions of images (b) (yellow), (c) (orange) and (d) (red).

For the cases at higher temperatures during rounds 4 and 5 much more significant nanostructuring was observed for the H+He cases, as in both cases a He fuzz [35] ring was grown centred on the plasma beam centre (Figure 8(e)). At 1150 °C the fuzz extends from a radius of ~1.6 to 3.3 mm with the thickest fuzz layer of up to ~1.5 µm around 2.4 mm radius as determined by SEM of FIB-prepared cross sections. The fuzz thickness

increases from around 20 nm at the outer radius up to 100-200 nm at the inner radius. Inside the inner radius some fuzz is still present but with less than 100% coverage of the surface and with increasingly thick tendrils. The centre of the laser spot is approximately co-located with the centre of the Magnum-PSI plasma beam (~1 mm from the centre of the plasma beam to the centre of the laser spot) and here the tendrils become very thick (>300 nm) and accompanied by small pores on the order of tens of nm. For the 1500 °C case the results are similar, but the fuzz ring extends from around a radius of 2.0 to 4.0 mm and the maximum thickness at 3.0 mm is around 3.0 µm (Figure 8(a)). It should be noted that in this case it is not precisely a ring as the fuzz extends further towards the edge of the monoblock, due to the higher temperature on that side from geometrical considerations. Inside the laser spot only pores in the W exist without any tendrils (Figure 8(b)). FIB-cuts indicate large pores several hundred nm in diameter underlie this region, though it appears there is a distribution from this size down to sizes below the detection limit of the images.

The formation of fuzz can be expected given the high electron temperatures in this case ($T_e = 6.1 \pm 0.4$ eV), unlike in [9]. The ring formation is due to the variable plasma potential as a function of the plasma radius, which results in a low ion energy at the beam centre and a higher one at the beam edge as $E_{ion} \approx k_B T_i + e(V_p - V_f)$ [36, 37]. Therefore the conditions for fuzz to form [38, 39] were bounded at the inner radius by the insufficient ion energy and at the outer radius by the insufficient surface temperature (Figure 8(f)). This is comparable to the transition expected in ITER from detached to attached conditions moving radially away from the strikepoint location, so incidentally these results may give some insight on what sort of fuzz might be expected to form if the conditions in ITER become favourable for this. The laser spot appears to have acted to accelerate the annealing process of the fuzz from tendrils to the formation of large voids due to the much higher surface temperatures in this region (e.g. compare Figure 8(b) to Figure 8(c)).

Overall again there was no modification in the damage category for the addition of seeding impurities compared to identical laser loading conditions in pure H plasma. Although we noted the category 'Surface modifications' in Figure 2 these occurred only in the laser damaged region, and were concluded to be a synergistic effect of the plasma and laser loading, the surface modifications here occurred both inside and outside the laser spot, and so we do not categorize these modifications as being a damage category due to the laser loading.

The influence of seeding was investigated with more granularity however by studying the measured surface roughness, S_q, for each case. These results are summarized in Figure 9. It can be clearly observed that once crack networks are formed (the three right-hand set of exposure conditions) the surface roughness increases by a factor of three or more, indeed up to a factor of ten for the case of $T_{base} + \Delta T$ = 1500+310 °C. Additionally in almost all cases the roughening is more pronounced for the case with seeding compared to the pure H case. This indicates a synergy between the modifications and nanostructuring caused by the plasma and the extent of the damage

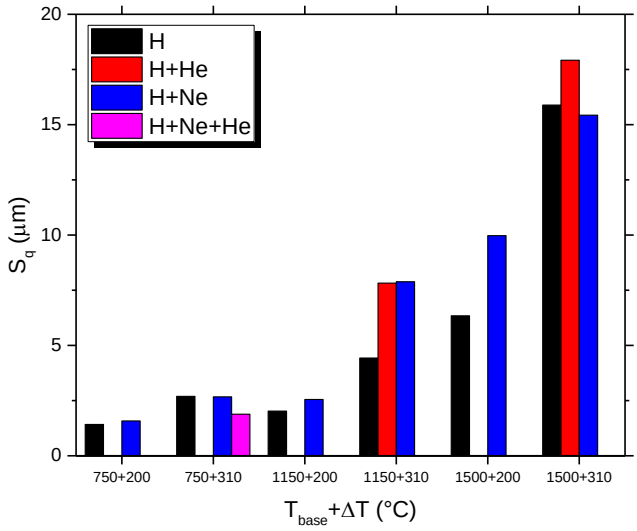

Figure 9: Bar chart of the measured S_q value for each seeded loading case compared to the identical pure H plasma loading case

caused by the transient heat loading. For the case at $T_{base} + \Delta T$ = 1500+310 °C the roughness increase is most pronounced but the differences are smaller between seeded and unseeded discharges, which suggests that the recrystallization and subsequent prominent crack-network formation may dominate over the influence from seeding impurities.

4. CONCLUSIONS AND IMPLICATIONS FOR ITER

In this paper two ITER monoblock mock-up chains were exposed to ELM-like loading and simultaneous H plasma loading in Magnum-PSI. Up to 10^6 ELM-like pulses simulated by laser exposure were applied at energies around the threshold for fatigue failure cracking, while surface temperature and seeding impurities were also varied as control parameters. Comparison of plasma and laser combined loading at 750 °C to data from electron beam loading at 700 °C [7] shows broadly similar conclusions for fatigue failure cracking thresholds, but indicates additional effects due to the plasma presence. It was also found that increasing the surface base temperature to 1150 °C or 1500 °C leads to a decrease in resistance to fatigue cracking from F_{HF} = 6.0 MW m^{-2} s$^{0.5}$ to below F_{HF} = 3.7 MW m^{-2} s$^{0.5}$. This behaviour was found to be in agreement with the Coffin-Manson relationship model for cycles to fatigue failure when fitted with empirical coefficients from literature [29, 30]. The recrystallization observed at 1500 °C also leads to more pronounced cracking and roughening, indicating a further acceleration in failure compared to that at 1150 °C. Lastly the addition of impurities lead to slightly more extensive surface modifications and strongly increased roughening for a given loading condition relative to that for pure H, indicating a clear synergy between the nanostructuring by the plasma and the damage caused by the thermal loading.

It is useful to try to draw some implications as to how these results can be used to better anticipate the divertor performance in ITER. Firstly compared to the earlier studies [4, 7] no small melt areas were seen here. This may imply that the edges were "rounded" by the plasma, but the mechanism for this remains unclear. From the He fuzz formation discussed in section 0 it can be concluded that sputtering would not play a role as the lack of He fuzz formation in the center of the sample limits the ion energy to below 20 eV [38]. Potentially the surface could be smoothed by surface adatom migration or deposition of impurities. Whether erosion is playing a role should be investigated however, as this would imply an unexpected material loss for ITER. It can be noted that no W emission was observed via OES, however, which implies a small upper limit for W erosion.

Secondly the fatigue damage threshold energy is lower than previously thought, by almost a factor of two, when the surface temperature is elevated from 750 °C to above 1150 °C. The temperatures here are comparable to those expected during the Fusion Power Operation phase of ITER [2]. Recent results [20] put the threshold for fatigue cracking for recrystallized tungsten at similar surface temperatures even lower, at F_{HF} = 2.0 MW m^{-2} s$^{0.5}$, equivalent to a parallel heat load from a type-I ELM of around $\varepsilon_{||}$ ~ 0.6 MJ m^{-2} following the scaling in [3]. This implies that avoiding surface cracking requires a mitigation factor of around 16-50 in reducing ELM size.

Lastly the finding that surface cracking leads to strong increases in surface roughness, and that this is enhanced by seeding impurity content, may give concern for surface erosion of tungsten, and may leave the surface more vulnerable to dust production (though likely very small compared to that expected from Be [40]), enhanced sputtering or local overheating, particularly at the low incidence angles expected in ITER [41].

Overall what is still not determined however is whether such surface cracking is acceptable for the ITER divertor or not. It seems challenging to reduce ELM parallel heat loads by very large factors to avoid this phenomenon entirely, so either fatigue cracking must be a tolerable outcome for the divertor or ELMs should be completely mitigated or avoided. In these experiments no macro-cracking arose due to surface cracking, however only a small region was loaded at a time and repeated thermal cycling at high heat loads was not carried out which could give rise to such deep cracks. This suggests value in determining to what extent surface cracking will impact the lifetime and reliability of the ITER divertor by more closely simulating this potential synergy.

5. ACKNOWLEDGEMENTS

We acknowledge the support of the Magnum-PSI Facility Team at DIFFER. The Magnum-PSI facility at DIFFER has been funded by the Netherlands Organisation for Scientific Research (NWO) and EURATOM. DIFFER is part of the institutes organisation of NWO. This work has been carried out within the framework of

the EUROfusion Consortium and has received funding from the Euratom research and training programme 2014-2018 and 2019-2020 under grant agreement No 633053. Work partly performed under EUROfusion WP PFC. The views and opinions expressed herein do not necessarily reflect those of the European Commission or of the ITER Organization.

6. REFERENCES

[1] GUNN, J.P. et al., Surface heat loads on the ITER divertor vertical targets, Nucl. Fusion **57** (2017).
[2] PITTS, R.A. et al., Physics basis for the first ITER tungsten divertor, Nucl. Mater. Energy **20** February (2019) 100696.
[3] EICH, T. et al., ELM divertor peak energy fluence scaling to ITER with data from JET, MAST and ASDEX upgrade, Nucl. Mater. Energy **12** (2017) 84.
[4] WIRTZ, M., LINKE, J., LOEWENHOFF, T., PINTSUK, G., UYTDENHOUWEN, I., Transient heat load challenges for plasma-facing materials during long-term operation, Nucl. Mater. Energy **12** January 2018 (2017) 148.
[5] HIRAI, T. et al., Status of technology R & D for the ITER tungsten divertor monoblock, J. Nucl. Mater. **463** (2015) 1248.
[6] LI, Y. et al., Fracture behavior of tungsten-based composites exposed to steady-state/transient hydrogen plasma, Nucl. Fusion **60** 4 (2020).
[7] LOEWENHOFF, T., LINKE, J., PINTSUK, G., THOMSER, C., Tungsten and CFC degradation under combined high cycle transient and steady state heat loads, Fusion Eng. Des. **87** 7–8 (2012) 1201.
[8] WIRTZ, M. et al., High pulse number thermal shock tests on tungsten with steady state particle background, Phys. Scr. **T170** T170 (2017) 014066.
[9] MORGAN, T.W. et al., ITER monoblock performance under lifetime loading conditions in Magnum-PSI, Phys. Scr. **2020** T171 (2020).
[10] HIRAI, T. et al., ITER tungsten divertor design development and qualification program, Fusion Eng. Des. **88** 9–10 (2013) 1798.
[11] BARABASH, V., "Material Specification for the Supply of Tungsten Plates for the ITER Divertor", ITER_D_2EDZJ4 v1.3 (10.03.2009).
[12] VAN ECK, H.J.N. et al., High-fluence and high-flux performance characteristics of the superconducting Magnum-PSI linear plasma facility, Fusion Eng. Des. **142** March (2019) 26.
[13] ARAKCHEEV, A.S. et al., Theoretical investigation of crack formation in tungsten after heat loads, J. Nucl. Mater. **463** (2015) 246.
[14] ARAKCHEEV, A.S. et al., Calculation of cracking under pulsed heat loads in tungsten manufactured according to ITER specifications, J. Nucl. Mater. **467** November (2015) 165.
[15] GIANNATTASIO, A., YAO, Z., TARLETON, E., ROBERTS, S.G., Brittle-ductile transitions in polycrystalline tungsten, Philos. Mag. **90** 30 (2010) 3947.
[16] YIN, C., TERENTYEV, D., PARDOEN, T., PETROV, R., TONG, Z., Ductile to brittle transition in ITER specification tungsten assessed by combined fracture toughness and bending tests analysis, Mater. Sci. Eng. A **750** February (2019) 20.
[17] ALFONSO, A., JUUL JENSEN, D., LUO, G.N., PANTLEON, W., Thermal stability of a highly-deformed warm-rolled tungsten plate in the temperature range 1100-1250 °c, Fusion Eng. Des. **98**–**99** (2015) 1924.
[18] SHAH, V. et al., Recrystallization behaviour of high-flux hydrogen plasma exposed tungsten, J. Nucl. Mater. **545** (2021).
[19] YU, J.H., DE TEMMERMAN, G., DOERNER, R.P., PITTS, R. a., VAN DEN BERG, M. a., The effect of transient temporal pulse shape on surface temperature and tungsten damage, Nucl. Fusion **55** 9 (2015) 093027.
[20] LI, Y. et al., Recrystallization-mediated crack initiation in tungsten under simultaneous high-flux hydrogen plasma loads and high-cycle transient heating, Nucl. Fusion **61** 4 (2021).
[21] BALDEN, M., ELGETI, S., MORGAN, T.W., BREZINSEK, S., DE TEMMERMAN, G., Scanning electron microscopy analyses of an ITER plasma-facing unit mockup exposed to extreme ion fluences in Magnum-PSI, Phys. Scr. **2020** T171 (2020).
[22] OSTRIKOV, K., Surface science of plasma exposed surfaces: A challenge for applied plasma science, Vacuum **83** 1 (2008) 4.
[23] MAIYA, P.S., Effects of surface roughness and strain range on the low-cycle fatigue behavior of type 304 stainless steel, Scr. Metall. **9** 11 (1975) 1277.

[24] JAVIDI, A., RIEGER, U., EICHLSEDER, W., The effect of machining on the surface integrity and fatigue life, Int. J. Fatigue **30** 10–11 (2008) 2050.
[25] SURARATCHAI, M., LIMIDO, J., MABRU, C., CHIERAGATTI, R., Modelling the influence of machined surface roughness on the fatigue life of aluminium alloy, Int. J. Fatigue **30** 12 (2008) 2119.
[26] VALBUSA, U., BORAGNO, C., BUATIER DE MONGEOT, F., Nanostructuring by ion beam, Mater. Sci. Eng. C **23** 1–2 (2003) 201.
[27] COFFIN, L.F.J., A study of the effects of cyclic thermal stresses on a ductile metal, Trans. ASTM **76** (1954) 931.
[28] MANSON, S.S., Fatigue: A complex subject—Some simple approximations, Exp. Mech. **5** 4 (1965) 193.
[29] SCHMUNK, R.E., KORTH, G.E., Tensile and low-cycle fatigue measurements on cross-rolled tungsten, J. Nucl. Mater. **104** C (1981) 943.
[30] SCHMUNK, R.E., KORTH, G.E., ULRICKSON, M., Tensile and low-cycle fatigue measurements on cross-rolled tungsten at 1505 K, J. Nucl. Mater. **122**&**123** (1984) 850.
[31] WIRTZ, M., LINKE, J., LOEWENHOFF, T., PINTSUK, G., UYTDENHOUWEN, I., Thermal shock tests to qualify different tungsten grades as plasma facing material, Phys. Scr. **2016** T167 (2016).
[32] WIRTZ, M. et al., Material properties and their influence on the behaviour of tungsten as plasma facing material, Nucl. Fusion **57** 6 (2017).
[33] YIN, C. et al., Tensile properties of baseline and advanced tungsten grades for fusion applications, Int. J. Refract. Met. Hard Mater. **75** April (2018) 153.
[34] SCHIJVE, J., Fatigue of Structures and Materials, 2nd ed., Springer Netherlands, Dordrecht (2009) 1–622 pp.
[35] TAKAMURA, S., OHNO, N., NISHIJIMA, D., KAJITA, S., Formation of Nanostructured Tungsten with Arborescent Shape due to Helium Plasma Irradiation, Plasma Fusion Res. **1** (2006) 051.
[36] COSTIN, C. et al., Cross-section analysis of the Magnum-PSI plasma beam using a 2D multi-probe system, Plasma Sources Sci. Technol. **24** (2015) 015014.
[37] COSTIN, C., ANITA, V., POPA, G., SCHOLTEN, J., DE TEMMERMAN, G., Tailoring the charged particle fluxes across the target surface of Magnum-PSI, Plasma Sources Sci. Technol. **25** 2 (2016) 025023.
[38] KAJITA, S., SAKAGUCHI, W., OHNO, N., YOSHIDA, N., SAEKI, T., Formation process of tungsten nanostructure by the exposure to helium plasma under fusion relevant plasma conditions, Nucl. Fusion **49** 9 (2009) 095005.
[39] DE TEMMERMAN, G., DOERNER, R.P., PITTS, R.A., A growth/annealing equilibrium model for helium-induced nanostructure with application to ITER, Nucl. Mater. Energy **19** January (2019) 255.
[40] TEMMERMAN, G. De et al., Data on erosion and hydrogen fuel retention in Beryllium plasma-facing materials, Nucl. Mater. Energy **27** October 2020 (2021) 100994.
[41] PITTS, R.A. et al., Physics conclusions in support of ITER W divertor monoblock shaping, Nucl. Mater. Energy **12** (2017) 60.